Available online at www.sciencedirect.com
ScienceDirect
Journal of the European Ceramic Society 30 (2010) 2003–2008
www.elsevier.com/locate/jeurceramsoc

Crystallization studies in mullite and mullite–YSZ beads

E. Garcia *, J. Mesquita-Guimarães, P. Miranzo, M.I. Osendi

Institute of Ceramics and Glass (ICV), CSIC, Madrid, Spain

Received 29 September 2009; received in revised form 30 March 2010; accepted 10 April 2010
Available online 4 May 2010

Abstract

Mullite and mullite/Y-ZrO_2 (25 and 50 vol.%) beads were produced by thermal spraying in water the corresponding atomised compositions. The amount of amorphous phases in the as-sprayed beads was comparatively determined by X-ray diffraction (XRD) and differential thermal analysis (DTA) methods. Characteristic XRD peaks associated to crystallization of the mullite and Y-ZrO_2 (t) phases were compared with the intensity of the exothermic events in the DTA for each composition. A direct linear relationship between the amount of amorphous phases estimated by XRD methods and the area under DTA peaks per unit mass was found. The crystallization microstructure of the different composition beads after heat treatments was followed by scanning electron microscopy (SEM).

Keywords: Mullite; ZrO_2; X-ray methods; Electron microscopy; Environmental barrier coatings

1. Introduction

Mullite based compositions find interesting applications in high temperature systems. In particular, for next generation of gas turbine engines with parts made of Si_3N_4 or SiC/SiC, which pursue higher working temperatures and efficiency, jointly with a lowering in fuel consumption and emission of green house effect gases. However, these appealing benefits can be hindered by the rapid degradation of those materials in the high temperature environment of gas turbines,[1–3] due to the reaction of the protective silica layer at their surface with the water vapor produced. In a similar way as thermal barrier coatings (TBC) have been used to protect metallic substrates against high temperatures, environmental barrier coatings (EBC) have been proposed to inhibit substrate corrosion in ceramic components. In this sense, mullite has been used as a transitional protective layer for Si-based components owing to its compatibility and close thermal expansion coefficient to these ceramics.[4–6] Mullite coatings processed by thermal spraying techniques normally become moderately amorphous, later crystallizing when heat-treated at $T \geq 1000\,^{\circ}C$, thus producing volume changes and frequently through coating cracks[7–9] that allow further oxidation. Moreover, even fully crystalline mullite coatings exhibited some volatilization of silica in water vapor rich atmospheres at high temperatures.[6–8] Different approaches have been attempted to solve this problem. Specifically, a ZrO_2–7–8 wt.% Y_2O_3 (YSZ) top coat was plasma sprayed over mullite[8,9] but the large mismatch in the coefficient of thermal expansion (CTE) between YSZ and mullite layers caused the fail of the system. Alternatively, special layered systems have been aimed looking for a reduction in thermal stresses through adjustment of CTE between consecutive layers.[9–12] Mathematical modeling of thermally activated time-dependent deformations in functionally graded zirconia-based TBCs has shown that the driving force for interface crack growth may be reduced by the addition of mullite.[13] Alongside, mullite/YSZ mixtures may play an important role as intermediate layers in mullite-based EBC coatings.

For these complex EBC systems, the study of the amorphous phase formation in thermal sprayed mullite/ZrO_2 compositions as well as the effect of ZrO_2 on the crystallization temperature onset are issues of great significance that can help in the successful design and performance understanding of these complex coatings. In the present work, we address these topics using X-ray diffraction (XRD) and differential thermal analysis (DTA) as basic tools. Instead of using thermal sprayed coatings as test specimens, we have chosen beads prepared by flame spraying compositions into water. These beads performed as powders and prevented phenomena like preferred orientation or the inter-

* Corresponding author. Tel.: +34 917355840; fax: +34 917355843.
E-mail address: garcia@icv.csis.es (E. Garcia).

0955-2219/$ – see front matter © 2010 Published by Elsevier Ltd.
doi:10.1016/j.jeurceramsoc.2010.04.018

ference of the substrate type on heat treatments. In thermally sprayed coatings, preferred orientation usually appears due to piling up of molten and re-solidified particles (splats) that can produce biased data. Observation of the beads surface after the heat treatments under the scanning electron microscope (SEM) helped to establish the specific crystallization microstructures.

2. Experimental

Mullite powders (Baikalox SASM, Baikowski Chemie, Annecy, France), with a purity of 99% and an average particle size of 1.3 μm, and zirconia stabilized with 7 wt.% Y_2O_3 (Y-TZP) powders (TZ4Y, Tosoh, Tokyo, Japan), 99.95% pure and with an average particle size of 0.3 μm, were the starting materials. Three different suspensions with 30 wt.% of solid content of mullite (M100), 75 vol.% mullite–25 vol.% Y-TZP (M75) and 50 vol.% mullite–50 vol.% Y-TZP (M50) were prepared. Suspensions were done in distilled water adding 0.4 wt.% of a polyelectrolyte dispersant (Dolapix CE 64 CA, Zschimmer-Schwarz, Lahnstein, Germany) and 5 wt.% of a polysaccharide binder (KB 1247, Zschimmer-Schwarz, Lahnstein, Germany), all contents are referred to the solid phase. The thoroughly mixing of all ingredients was assured by using a blade mixer and, subsequently, a continuous attrition mill. Owing to their nature, none of the additives left residues after thermal spraying.

The slurries were spray dried with a rotary atomizer spray dryer (Mobile Minor, Niro Atomizer, Søborg, Denmark) in a co-current flow. Beads were made by flame spraying (FS) corresponding batches of spray dried (SD) powders using an oxygen–acetylene gun (model CastoDyn DS 8000, Eutectic Castolin, Madrid, Spain) into a water filled metal container, at the stand-off distance of 15 cm. Beads were drained and oven dried at 120 °C. To study crystallization, beads were furnace treated at 1000 and 1300 °C for 1 h.

Particle size distributions of the SD powders and as-sprayed beads were determined with a laser diffraction analyzer (Mastersizer S, Malvern, UK). The morphology of the different powders was studied with the SEM (DMS-950 Carl-Zeiss, Oberkochen, Germany). XRD were performed using a Xpert PRO diffractometer (PANalytical, NL) with a $\theta/2\theta$ configuration, in the 10–70° 2θ range, with a step of 0.0165°, a time per step of 50 s and 15 rpm of sample spinning. The DTA was performed with a Simultaneous Thermal Analyzer of Netzch, model 409 (Germany), at a heating rate of 10 °C/min, using alumina standard.

3. Results and discussions

SEM micrographs of the SD agglomerates and the corresponding FS beads are shown in Fig. 1. The SD agglomerates show mostly round porous particles, whereas the beads are compact spheres with a narrower size distribution. The average particle size of SD powders and FS beads was around 26 μm for all compositions as it is reflected in Table 1. In the case of M50 beads, crystallizations are evidenced on the particle surface (Fig. 1(f)).

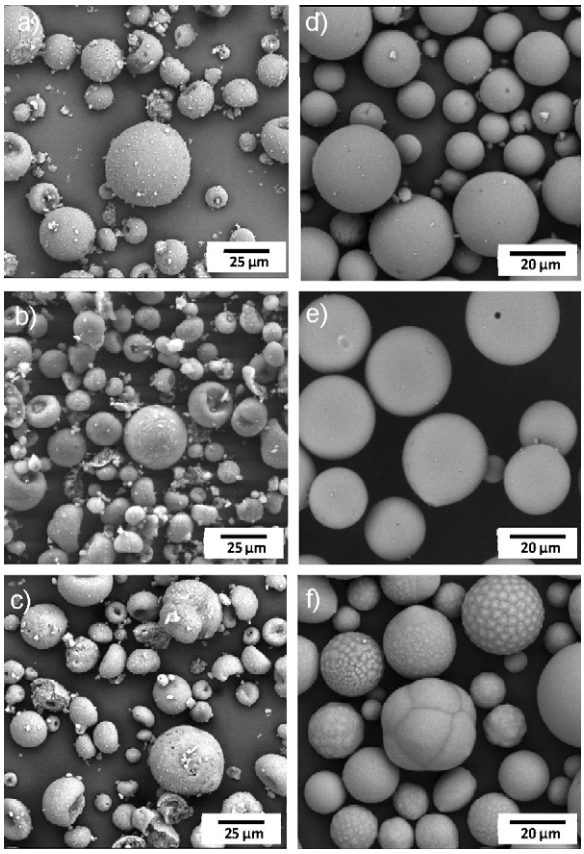

Fig. 1. SD agglomerates and corresponding FS beads of (a and d) M100, (b and e) M75 and (c and f) M50 compositions.

XRD patterns of SD powders and FS beads for the three compositions are compared in Fig. 2 where strong reductions in peaks intensity for the FS beads are evident. M100 SD powders show typical peaks of mullite, whereas M75 SD and M50 SD show intense diffraction peaks of t-ZrO_2 and weak mullite peaks. Furthermore, M100 FS beads show a hump at ∼26° (2θ) indicating the presence of amorphous mullite (Fig. 2(a)); conversely, M50 FS beads present sharp diffraction peak of t-ZrO_2 but mullite diffraction peaks are not detected (Fig. 2(c)). Finally, M75 FS beads are predominantly amorphous (Fig. 2(b)), with a shoulder around 30° (2θ), which corresponds to the maximum intensity peak of t-ZrO_2. The higher amorphisation detected in this composition can be explained by its proximity to the eutectic point of the Al_2O_3–SiO_2–ZrO_2 phase equilibrium diagram[14] as depicted in Fig. 3. Even though thermal spraying methods are very dynamical process, phase equilibrium thermodynamics establishes that eutectic composition is completely melted when eutectic temperature is reached and conversely, on cooling, crystallization occurs at that temperature. Therefore, compositions

Table 1
Average particle size of SD powders and beads.

Composition	SD d_{50} (μm)	FS d_{50} (μm)
M100	26	30
M75	26	28
M50	23	27

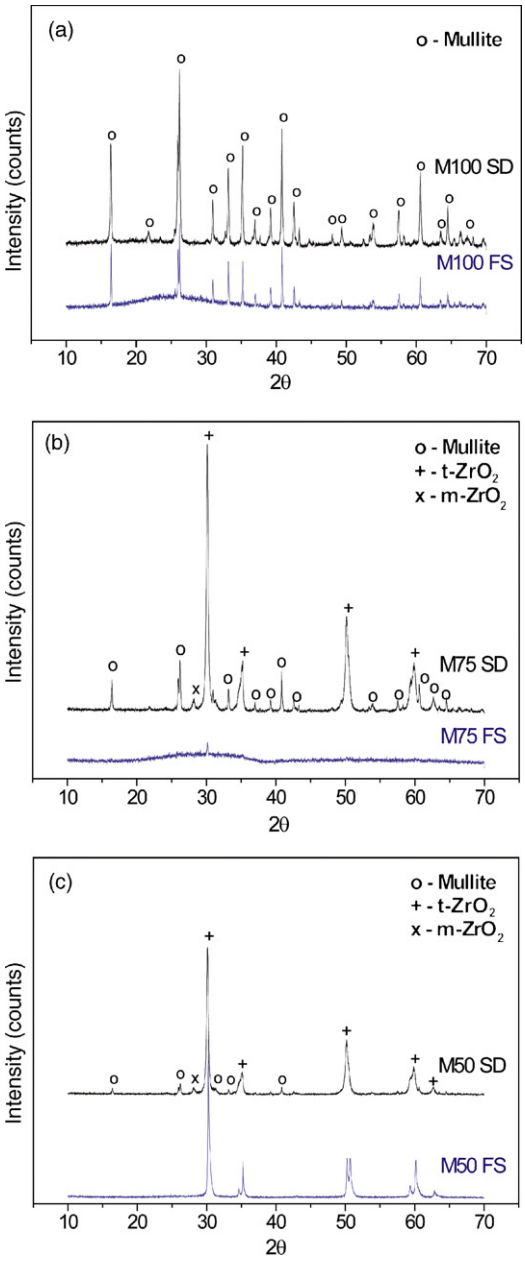

Fig. 2. XRD patterns of the SD and FS powders (a) M100, (b) M75 and (c) M50.

close to the eutectic would be more prone to achieve melting during the short flying time.

In Fig. 4, DTA thermographs of the three compositions show one exothermic peak around 1000 °C. This peak is sharper and stronger in the M100 FS than in the composite FS beads (Fig. 4(a)). Besides, M75 and M50 FS beads present a less intense second exothermic peak around 1200–1250 °C (Fig. 4(b)). Whereas the later peak is associated to second mullite crystallization in Al_2O_3–SiO_2 mixtures,[15] the first has been alternatively ascribed to Al–Si spinel, γ-Al_2O_3 or even incipient mullite formation.[16,17] More recent studies suggest that the previous thermal history of Al_2O_3–SiO_2 gels and melts determines the mullite crystallization path.[18,19]

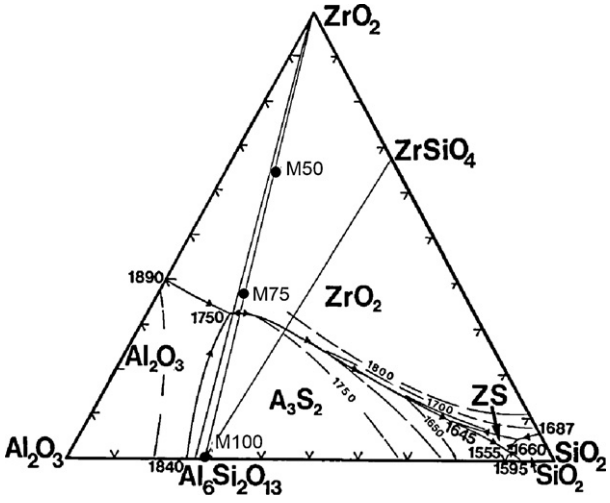

Fig. 3. Al_2O_3–SiO_2–ZrO_2 phase equilibrium diagram[14] showing the location of the M100, M75 and M50 compositions.

The area under the DTA peaks divided by the mass used for the analysis (∼50 mg) (A_{DTA}) gives a notion of the energy involved in the crystallization process of each composition. The following figures were obtained for A_{DTA}: 94 (M100), 102 (M75) and 28 (M50) (in μV s/mg units). A_{DTA} of the M75 FS beads was the largest in agreement with the higher amount of amorphous phase in this composition as it was shown in the XRD patterns (Fig. 2(b)).

Following DTA results, FS beads were heat treated at 1000 and 1300 °C for 1 h and subsequently, XRD patterns were recorded (see Fig. 5(a)–(c)). An increase in the intensity of XRD peaks as compared to the as-sprayed beads is observed in all compositions. For the 1300 °C treatment, patterns are rather similar to the original SD powders, and specimens can be considered as totally crystallized. If comparison between XRD patterns of 1000 and 1300 °C treatments are done, it comes clear that M100 is quite crystallized at 1000 °C, owing to the similar intensity of mullite diffraction peaks. However, the single peak at 26° (2θ) in the 1000 °C pattern (enlarged view in Fig. 5(a)) can be attributed to a pseudotetragonal mullite, in agreement with Johnson et al.[19] that observed this transitional mullite in heat treated glass mul-

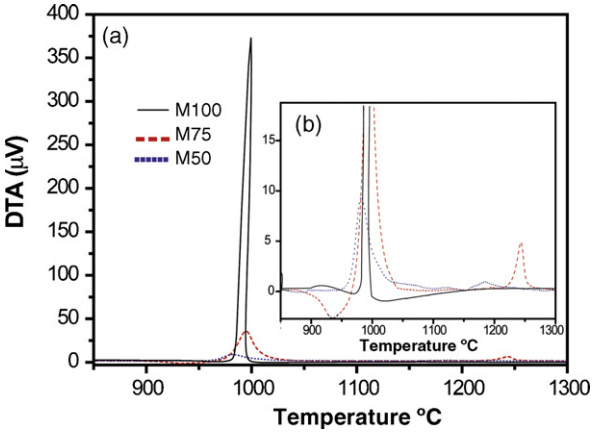

Fig. 4. DTA thermographs of the given compositions (a) and a detail where secondary exothermic peaks appear enlarged (b).

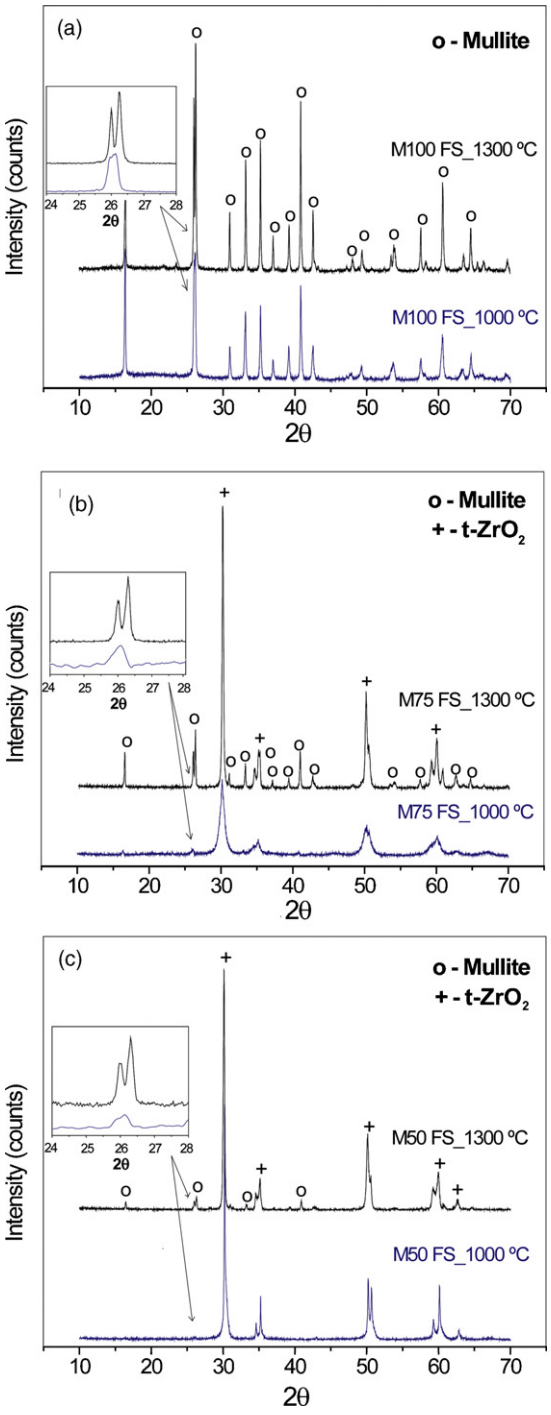

Fig. 5. XRD patterns of heat treated beads of the different compositions (a) M100, (b) M75 and (c) M50). Enlarged views of the 24°–28° zone are included.

lite beads for temperatures below 1200 °C. This peak splits in the XRD pattern of M100 beads heated at 1300 °C (see detail in Fig. 5(a)), which confirms the orthorhombic mullite formation. Nevertheless, in the composite beads the fully crystallized pattern is only recovered at 1300 °C, especially for the mullite peaks showing now the doublet peak at 26° (2θ) (enlarged view in Fig. 5(b) and (c)).

To get a quantitative estimation of the amount of amorphous phases in the beads, we have defined the crystallinity ratio (C.R.)

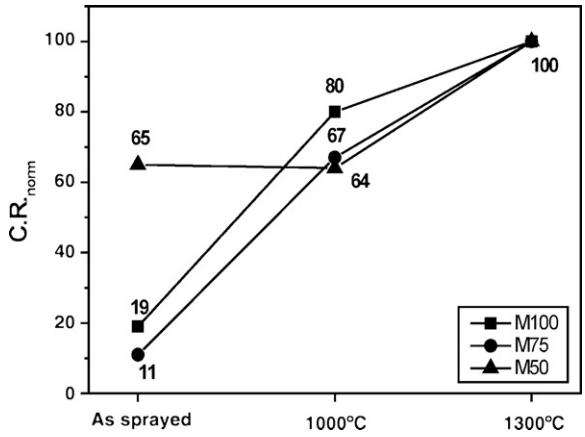

Fig. 6. Normalized C.R. as a function of thermal treatment temperature.

as a parameter that relates the area under the XRD peaks to the total area under the diffraction pattern,

$$\text{C.R.} = \frac{A_{\text{peaks}}}{A_{\text{curve}}} \times 100 \quad (1)$$

where A_{curve} is the area under a specific segment of the XRD pattern and A_{peaks} is the area under the peaks present in that segment. In here, the area was integrated in 2θ between 20° and 40°, because it is the representative range where the amorphous humps and the significant XRD peaks are located. To get the area under the peaks, the base-line was subtracted and the peaks were fitted to Lorentzian curves. Subsequently, the C.R. was normalized (C.R.$_{\text{norm}}$) to the corresponding values for the samples treated at 1300 °C, i.e. the fully crystallized specimens, giving thus an estimate of the amorphous phase content as 100-C.R.$_{\text{norm}}$.

A clue of how C.R.$_{\text{norm}}$ evolves as a function of the heat treatments can be appraised in Fig. 6, for the three compositions. In Table 2, the area ratio between the diffraction peaks of mullite and ZrO_2 are reflected for the two mix compositions to give a comparative indication of the weight of each phase. As seen in Fig. 6, for the as-sprayed state, M75 composition shows the lowest C.R.$_{\text{norm}}$ (11%) and M50, the highest (65%), probably because ZrO_2 rapidly nucleates in this specimen (Fig. 1(f)). The increase in C.R.$_{\text{norm}}$ for M100 composition after heating at 1000 °C is ~60%, which should be associated to pseudotetragonal mullite crystallization in view of the XRD results (Fig. 5(a)). For M75 a similar increase is observed although it seems mostly

Table 2
Ratio between the areas of mullite diffraction peaks (A_{mullite}) and ZrO_2 diffraction peaks (A_{ZrO_2}) in 20–40° range (2θ) for M75 and M50 samples. Data for original spray dry powders (SD), as-sprayed beads (FS) and heat treated specimens.

	$A_{\text{mullite}}/A_{ZrO_2}$	
	M75	M50
SD	0.2	0.07
FS	0	0
1000 °C	0.02	0
1300 °C	0.3	0.07

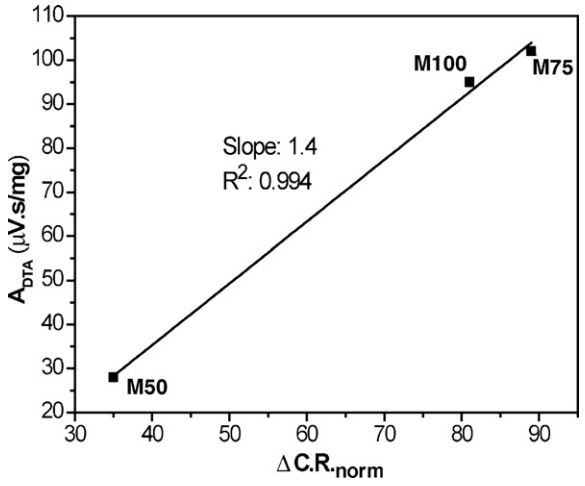

Fig. 7. DTA area per unit mass (A_{DTA}) versus the increment in the crystallinity ratio ($\Delta C.R._{norm}$).

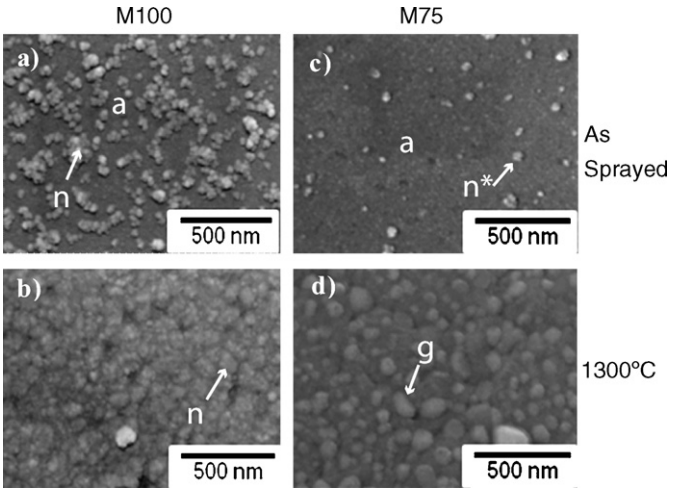

Fig. 8. SEM micrographs of M100 and M75 beads surface for the as-sprayed and 1300 °C treatment. Amorphous continuous phase is labeled as "a", the different nuclei as "n" and "n*"and grains as "g". See text for explanation.

linked to ZrO_2 crystallization as shown in Table 2 and Fig. 5(b), where the intensity ratio between mullite and ZrO_2 peaks (0.02) is far from the value of the crystallized composition (0.2–0.3). Finally, the $C.R._{norm}$ increase for M50 after heating at 1000 °C is almost negligible (3%), confirming that ZrO_2 mostly nucleates in the as-sprayed specimen and mullite has hardly crystallized at 1000 °C (Table 2 and Fig. 5(c)). Actually, heating up to 1300 °C was necessary to get entire mullite crystallization in M50 (Fig. 6). Therefore, ZrO_2 seems to hamper crystallization of the pseudotetragonal mullite at 1000 °C, maybe due to the extra disorder added by the Zr atoms in the Al_2O_3–SiO_2 glass network, shifting the crystallization temperature range to higher temperatures and directly forming the orthorhombic mullite. It is known that the level of atomic mixing in Al_2O_3/SiO_2 mixtures determines the nucleation temperature of mullite, which can move from 1000 °C to ~1280 °C.[15,18,19]

To correlate the expected increase in crystallization from the as-sprayed to the fully crystalline state with the DTA exothermic effect, A_{DTA} versus $\Delta C.R._{norm} = (C.R._{norm})_{1300} - (C.R._{norm})_{as\text{-}sprayed}$ is represented in Fig. 7 for the three compositions. The plot shows a linear relationship ($R^2 = 0.994$) between both parameters. Therefore, just by doing a simple DTA and introducing the value in the plot, the amount of amorphous phase in any mullite/ZrO_2 mixture thermally sprayed may be estimated, with a minimum detection limit ~20%, as extrapolated from Fig. 7.

Detailed views of the as-sprayed and heat treated M100 and M75 beads surface are offered in Fig. 8. For as-sprayed mullite (Fig. 8(a)) a continuous amorphous-like phase ("a" label) with some inlaid nuclei ("n") of about 50 nm are seen. After heat treating at 1300 °C (Fig. 8(b)), the number of nuclei has markedly increased but maintaining their size. In as-spayed M75 beads (Fig. 8(c)), a continuous amorphous phase with few nuclei ascribed to t-ZrO_2 ("n*") are seen. Smaller number of nuclei than in M100 beads is observed in accordance to its lower crystallinity. At 1300 °C (Fig. 8(d)), microstructure seems like homogenous composite of two fine grained phases (~100 nm), the white grains ("g") being of ZrO_2.

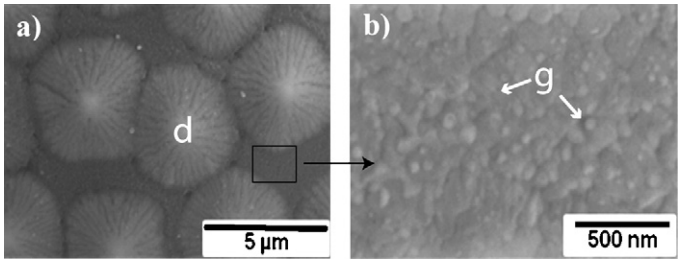

Fig. 9. SEM micrographs of M50 beads surface for the 1300 °C heat treatment (a) and a higher magnification detail (b). ZrO_2 dendrites ("d") are clearly seen (a) and small grains ("g") of mulite and ZrO_2 are observed in the enlarged view (b).

Conversely, M50 beads show distinct features (Fig. 9) to the other two, probably because this composition is in the primary crystallization field of ZrO_2 and closer than M75 to the ZrO_2 corner, which produces the rapid nucleation of t-ZrO_2 crystals even during the fast cooling of the thermal spraying in water. Patterns of ZrO_2 dendrites were distinguished in as-sprayed beads, which remained unchanged after heat treatments at 1000 and 1300 °C, see "d" in Fig. 9(a). Besides, at 1300 °C the nucleation of mullite and some tiny ZrO_2 grains ("g" in Fig. 9(b)) among the dendrite crystals is perceived.

4. Conclusions

The degree of crystallization of flame sprayed mullite/ZrO_2 beads depends on the particular composition of the mixture. Compositions close to the eutectic, 75 Mullite–25 ZrO_2 vol.%, were mostly amorphous after spraying. In general, the presence of ZrO_2 in the bead composition shifted mullite crystallization to higher temperatures (~1200 °C). A crystallinity parameter was defined from the XRD patterns that linearly correlates with the area under exothermic crystallization peaks of the DTA graph. This simple correlation can be used to estimate the amount of amorphous phase in thermal sprayed mullite/ZrO_2 mixtures when the content exceeds 20%.

Acknowledgments

This work was funded by the NRC-CSIC Cooperation program (project 2007CA003). Financial support of Spanish Ministry of Science and Innovation (MCINN) under project MAT2006-7118 is also recognized. Eugenio Garcia acknowledges the Ramón y Cajal Program for his financial support.

References

1. Robinson RC, Smialek JL. SiC recession caused by SiO_2 scale volatility under combustion conditions. I. Experimental results and empirical model. *J Am Ceram Soc* 1999;**82**:1817–25.
2. Smialek JL, Robinson RC, Opila EJ, Fox DS, Jacobson NS. SiC and Si_3N_4 recession due to SiO_2 scale volatility under combustor conditions. *Advanced Composite Materials: The Official Journal of the Japan Society of Composite Materials* 1999;**8**:33–45.
3. More KL, Tortorelli PF, Ferber MK, Keiser JR. Observations of accelerated silicon carbide recession by oxidation at high water-vapor pressures. *J Am Ceram Soc* 2000;**83**:211–3.
4. Ueno S, Jayaseelan DD, Ohji T. Development of oxide-based EBC for silicon nitride. *Int J Appl Ceram Technol* 2004;**1**(4):362–73.
5. Kimmel J, Miriyala N, Price J, More K, Tortorelli P, Eaton H, Linsey G, Sun E. Evaluation of CFCC liners with EBC after field testing in a gas turbine. *J Eur Ceram Soc* 2002;**22**:2769–75.
6. Krishnamurthy R, Sheldon BW, Haynes JA. Stability of mullite protective coatings for silicon-based ceramics. *J Am Ceram Soc* 2005;**88**:1099–107.
7. Ueno S, Ohji T, Lin HT. Corrosion and recession of mullite in water vapor environment. *J Eur Ceram Soc* 2008;**28**:431–5.
8. Lee KN, Miller RA. Development and environmental durability of mullite and mullite/YSZ dual layer coatings for SiC and Si_3N_4 ceramics. *Surf Coat Technol* 1996;**86**:142–8.
9. Lee KN. Current status of environmental barrier coatings for Si-based ceramics. *Surf Coat Technol* 2000;**133–134**:1–7.
10. More KL, Tortorelli PF, Walter LR, Kimmel JB, Miriyala N, Price JR, Sun EY, Linsey GD. Evaluating environmental barrier coatings on ceramic matrix composites after engine and laboratory exposures, *ASME paper 2002-GT-30630*, IGTI 4 A, p. 155–162.
11. Lee KN, Fox DS, Bansal NP. Rare earth silicate environmental barrier coatings for SiC/SiC composites and Si_3N_4 ceramics. *J Eur Ceram Soc* 2005;**25**:1705–15.
12. Spitsberg I, Steibel J. Thermal and environmental barrier coatings for SiC/SiC CMCs in aircraft engine applications. *Int J Appl Ceram Technol* 2004;**1**:291–301.
13. Rangaraj S, Kokini K. Interface thermal fracture in functionally graded zirconia–mullite-bond coat alloy thermal barrier coatings. *Acta Mater* 2003;**51**:251–67.
14. Pena P, De Aza S. The zircon thermal behaviour: effect of impurities. *J Mater Sci* 1984;**19**:135–42.
15. Yoldas BE. Effect of ultrastructure on crystallization of mullite. *J Mater Sci* 1992;**27**:6667–72.
16. Hoffman DW, Roy R, Komarneni S. Diphasic xerogels, a new class of materials: phases in the system Al_2O_3–SiO_2. *J Am Ceram Soc* 1984;**67**:468–71.
17. Srikrishna K, Thomas G, Martinez R, Corral MP, De Aza S, Moya JS. Kaolinite–mullite reaction series: a TEM study. *J Mater Sci* 1990;**25**:607–12.
18. Tkalcec E, Nass R, Nass, Schmauch J, Schmidt H, Kujarica S, Bezjak A, Ivankovik H. Crystallization kinetics of mullite from single-phase gel determined by isothermal differential scanning calorimetry. *J Non-Cryst Solids* 1998;**223**:57–72.
19. Johnson BR, Kiriven WM, Schneider J. Crystal structure development during devitrification of quenched mullite. *J Eur Ceram Soc* 2001;**21**:2541–62.